Decreasing subseasonal temperature variability in the northern extratropics attributed to human influence

Russell Blackport[1*], John C. Fyfe[1] & James A. Screen[2]

[1]Canadian Centre for Climate Modelling and Analysis, Environment and Climate Change Canada, Victoria, BC, Canada

[2]College of Engineering Mathematics and Computer Science, University of Exeter, Exeter, UK

*Corresponding author email: russell.blackport@canada.ca

Changes in subseasonal temperature variability are linked with the altered probability of weather extremes and have important impacts on society and ecological systems. Earlier studies based on observations up to 2014 have shown a general decrease in subseasonal temperature variability over Northern Hemisphere extratropical land. However, these changes have been confined to specific regions and seasons, have limited statistical significance, and human influence is yet to be determined. Here we show using up-to-date observations and climate model simulations that a human fingerprint, or pattern, of change in subseasonal variability has recently emerged over the Northern Hemisphere extratropics. The fingerprint features decreased near-surface air temperature variability over land in the high-northern latitudes in autumn, further extending into mid-latitudes in winter. Using large ensembles of single-forcing model experiments, we attribute the pattern of reduced temperature variability primarily to increased anthropogenic greenhouse gas concentrations, with anthropogenic aerosols playing a secondary role. Our results reveal that human influence is now detectable in hemispheric-wide day-to-day temperature variability

and motivates research into the impacts of reduced temperature volatility on societal and ecological systems.

Main

While the human influence on time averaged temperature changes is unequivocal[1], the influence on day-to-day (or week-to-week, and so on) temperature variability is less certain. Observations over recent decades show trends in subseasonal temperature variability that vary by region and season. Reductions in temperature variability have been observed over the northern high-latitudes in autumn[2] and over North America in both winter[3] and summer[4], while increased variability has been observed over Eurasia during summer[4]. Human influence on temperature variability has yet to be determined, but is expected to depend on various processes including changes in thermal advection linked to altered background temperature gradients[2,5–7], atmospheric circulation variability[8], snow cover extent[9], and soil moisture-temperature feedbacks[10].

Climate models forced with projected increases in greenhouse gas concentrations show a robust decrease in subseasonal temperature variability over the mid-to-high latitudes, during all seasons except summer[2]. This decrease in variability has been attributed in some studies to the reduction of temperature gradients associated with the faster warming of Arctic compared with lower latitudes[2,5,7,11], also known as Arctic amplification. In contrast, other studies have argued that temperature variability in the mid-latitudes could increase due to Arctic-forced changes in atmospheric circulation variability[12–14]. It has also been suggested that models may not accurately capture these potential circulation responses to Arctic warming[15], calling into question the projected decrease in temperature variability.

In this study, we apply tried-and-tested formal detection methods to identify the human fingerprint of subseasonal temperature variability in observations over the 1979-2020 period. The fingerprint is determined from the spatial pattern of the subseasonal temperature variability response to external forcing in large ensembles of simulations from two climate models. We find that the fingerprint has recently become detectable above internal variability in observations during autumn and winter. Using simulations that isolate individual climate drivers, we then attribute the observed reduction in temperature variability primarily to anthropogenic greenhouse gas emissions.

Trends in subseasonal temperature variability

We start by examining spatial maps of linear trends in subseasonal near-surface temperature variability over land from 1979-2020 in two reanalysis datasets (ERA5 and NCEP-DOE reanalysis 2). The temperature variability is determined by calculating the standard deviation of daily temperature anomalies for each season, resulting in a 41-year time series at each grid point (see Methods). During autumn (September-October-November; SON), both reanalyses show statistically significant decreases over Northern Canada and Northern Eurasia (Fig 1a,c). In winter (December-January-February; DJF), the decreases in temperature variability extend further into to the mid-latitudes, covering most of North America and Eurasia (Fig 1b,d). The two reanalyses depict highly similar spatial patterns of trends, but the magnitude of the variability reduction is greater in the NCEP reanalysis.

To check whether the trends seen in the reanalyses accurately reflect observed trends, we also examined trends from the Berkeley Earth daily gridded temperature data (Extended Data Fig. 1). Over the common time period (data were only available up to winter 2018 for Berkeley Earth data), there is strong agreement in trends between gridded observations and reanalyses, particularly with ERA5. This gives high confidence that the trends in the reanalyses faithfully capture observed changes.

To test whether the trends could be externally forced (e.g. from increasing greenhouse gas concentrations in the atmosphere), we examine analogous trends in subseasonal temperature variability from model simulations with observed historical forcings over 1979-2005 and then projected forcings from 2006-2020. We use large ensembles of simulations from two Earth System Models (CanESM2 and CESM1) to test the robustness of the projected changes. Both models show ensemble-mean reductions in temperature variability over mid- and high-latitudes, in agreement with the reanalyses (Fig 1e-h). The modelled trends show a smoother spatial structure compared to reanalysis, which is expected because internal variability is averaged out when taking an ensemble mean. Both models show similar seasonality of trends compared to the reanalyses, with reduced variability largely confined to the high latitudes in autumn, but extending into the mid-latitudes in winter. The similarity of the simulated trends (which consist of only the forced response) to observed trends (which consist of both a forced component and internal variability), suggests that the observed trends may reflect a forced response. In the next section, we will determine whether this forced trend seen in the models has emerged above the background internal variability in observations.

In Extended Data Fig. 2, we show the subseasonal temperature variability trends, in reanalyses and models, in spring (March-April-May; MAM) and summer (June-July-August; JJA). Both simulated and observed trends are weaker in these seasons, but the models show reduced temperature variability over high latitudes during spring, and weakly increased temperature variability over the high latitudes in summer. Compared to autumn and winter, there is less consistency in the spatial pattern of the trends in temperature variability across the reanalyses, and between the reanalyses and models. The weaker signals in spring and summer likely results from the different physical processes that drive changes temperature variability during these seasons. Because of these weaker trends in spring and summer, we will focus on autumn and winter for the rest of the analysis.

Fingerprint analysis

The strong similarity in the observed and simulated trend patterns motivates a fingerprint analysis to determine whether human influence is detectable in observations. We use standard fingerprinting methods that have been used to detect human influence on many aspects of the climate system (see Methods)[16–18]. First, we define the fingerprints to be the leading Empirical Orthogonal Function (EOF) from the ensemble-mean temperature variability anomalies (relative to climatology) of each of the two models. These are shown in the Extended Data Fig. 3, but are nearly identical in pattern to the linear trends shown Fig. 1e-h. Next, we calculate the signal time-series, by projecting the temperature variability anomalies from the reanalyses and observations onto the model fingerprints. Figure 2 shows these signal time-series in autumn and winter, using the fingerprints defined from each model. In both autumn and winter, all signal time-series generally increase over the past 41 years, indicating growing similarity of observed anomalies to the model fingerprints. The different reanalyses and observations are in good agreement on the trend and interannual variability of the signal time-series, again providing confidence in robustness of the result.

We next examine whether the signals of the fingerprint (from Fig. 2) have emerged above the background noise. We calculate signal-to-noise ratios by comparing the magnitude of trend in the signal time-series to the standard deviation of the magnitude of trends of the same length from time series containing only noise (see Methods). Figure 3 shows the signal-to-noise ratios, for increasing trend length starting in 1979, calculated separately using the fingerprint from each model. In autumn, the observed signal-to-noise ratios became statistically significant (at the 5% level) between 2005 and 2007, depending on the observational/reanalysis product and model used to determine the fingerprint. Over the 1979 to 2019 period, the fingerprint is highly detectable in both reanalyses with signal-to-noise ratios ranging from 4.7 to 5.3. In winter, the time of detection has a stronger dependence on the observations and model used, with time of detection ranging from 2005 to 2018. However, regardless of the observations and model used, the signal-to-noise ratio is statistically significant for trends ending in 2020, with signal-to-noise ratios ranging from 2.5 to 3.7. Also shown in Figure 3 are the signal-to-noise ratios from the individual realizations of the models. The observations and reanalyses fit within the ensemble range, indicating that the magnitudes of their changes are within the model spread.

So far, our analysis has only examined the temperature variability over land because the reanalysis data over land is likely better constrained by observations, and because the daily observational data from Berkeley Earth only includes land stations. Keeping the uncertainty of the reanalysis data in mind, we found that signal-to-noise ratios are even higher if ocean regions are included in the analysis (Extended Data Fig. 4), because both the reanalyses and models show strong reductions in subseasonal temperature variability over high-latitude ocean regions near the sea ice edge (Extended Data Fig 5).

Attribution to human influence

We now use single-forcing large-ensemble experiments to attribute the externally forced response of subseasonal temperature variability to individual climate drivers. In response to only increased anthropogenic greenhouse gas concentrations, both models show reduced temperature variability (Fig 4a-d) similar to that in the historical experiment (pattern correlations range from 0.71 to 0.93, depending on model and season), indicating that the anthropogenic greenhouse gases are the primary driver of the forced response. In autumn, both models also show reduced temperature variability in high latitudes in response to anthropogenic aerosol reductions over recent decades. The spatial pattern of the autumn response to aerosol forcing is similar to that to greenhouse gas forcing (pattern correlations of 0.50 and 0.75 in CanESM2 and CESM1 respectively), but with weaker magnitude. In winter, there is less consistency in the responses to aerosols between the two models, which partly explain the minor differences in the winter responses to historical forcing in the two models (Fig. 1f, h).

Previous work has attributed reduced temperature variability in model projections to the decreased meridional temperature gradients associated with Arctic amplification[2,5]. This is supported by targeted modelling experiments forced with imposed sea ice loss and Arctic amplification in isolation[7,11,19–22]. Consistent with this interpretation, our simulations display seasonal-mean warming (Extended Data Fig. 6) and reduced meridional temperature gradients (Extended Data Fig. 7). In response to greenhouse gas forcing only, there is clear Arctic amplification and associated reduced meridional temperature gradients, which have similar spatial patterns to the reduced temperature variability. Furthermore, aerosol forcing has also caused amplified warming in the Arctic, leading to reduced meridional temperature gradients. Other processes such decreases in land-sea temperature gradients[6] and decreases in snow cover extent[9] may also contribute to the decrease in temperature variability.

Implications for future change

There has been considerable disagreement, between model-based and observation-based studies, on the response of midlatitude circulation and winter temperature extremes to Arctic amplification[15]. However, we find a convergence between modelled and observed trends in subseasonal winter temperature variability, increasing confidence in model projections. Consistent with previous investigations into the mechanisms[2,5,7,11,19–22], we have shown that temperature variability is linked to changes in the large-scale meridional temperature gradients[5], which are highly similar in observations and models. The human influence on atmospheric circulation variability, which is undetectable in observations[23] and inconsistent between models[24], likely plays a smaller role.

Our results demonstrate that human influence on climate is now detectable in subseasonal temperature variability, not only in shifts in climate averages. The narrowing of the distribution of daily temperatures that we find implies that cold extremes are becoming less frequent and less severe at a faster rate than predicted by the shift in mean temperature; and conversely, hot extremes are becoming more frequent and more severe at a slower rate than predicted by a shift in the mean. However, changes in higher order moments of the temperature distribution[8,25], such as skewness and kurtosis that were not examined here, could also contribute to frequency and severity of extremes. The reduced temperature variability we have detected over recent decades is expected to continue with ongoing greenhouse gas emissions[2]. Our work encourages investigation into the impacts of human-induced changes in temperature variability on society and ecosystems[26–29].

References

1. Stocker, T. F. Climate Change 2013: The Physical Science Basis: Contribution of Working Group I to the Fifth Assessment Report of the Intergovernmental Panel on Climate Change. (Cambridge Univ. Press, 2013).

2. Screen, J. A. Arctic amplification decreases temperature variance in northern mid- to high-latitudes. Nat. Clim. Change **4**, 577–582 (2014).

3. Rhines, A., McKinnon, K. A., Tingley, M. P. & Huybers, P. Seasonally Resolved Distributional Trends of North American Temperatures Show Contraction of Winter Variability. J. Climate **30**, 1139–1157 (2017).

4. McKinnon, K. A., Rhines, A., Tingley, M. P. & Huybers, P. The changing shape of Northern Hemisphere summer temperature distributions. Journal of Geophysical Research: Atmospheres **121**, 8849–8868 (2016).

5. Schneider, T., Bischoff, T. & Płotka, H. Physics of Changes in Synoptic Midlatitude Temperature Variability. J. Clim. **28**, 2312–2331 (2015).

6. De Vries, H., Haarsma, R. J. & Hazeleger, W. Western European cold spells in current and future climate. Geophysical Research Letters **39**, (2012).

7. Dai, A. & Deng, J. Arctic Amplification Weakens the Variability of Daily Temperatures over Northern Middle-High Latitudes. Journal of Climate **34**, 2591–2609 (2021).

8. Linz, M., Chen, G. & Hu, Z. Large-Scale Atmospheric Control on Non-Gaussian Tails of Midlatitude Temperature Distributions. Geophysical Research Letters **45**, 9141–9149 (2018).

9. Fischer, E. M., Lawrence, D. M. & Sanderson, B. M. Quantifying uncertainties in projections of extremes—a perturbed land surface parameter experiment. Clim Dyn **37**, 1381–1398 (2011).

10. Fischer, E. M., Rajczak, J. & Schär, C. Changes in European summer temperature variability revisited. Geophysical Research Letters **39**, (2012).

11. Collow, T. W., Wang, W. & Kumar, A. Reduction in Northern Midlatitude 2-m Temperature Variability due to Arctic Sea Ice Loss. J. Climate **32**, 5021–5035 (2019).

12. Francis, J. A. & Vavrus, S. J. Evidence linking Arctic amplification to extreme weather in mid-latitudes. Geophys. Res. Lett. **39**, L06801 (2012).

13. Francis, J. A. & Vavrus, S. J. Evidence for a wavier jet stream in response to rapid Arctic warming. Environ. Res. Lett. **10**, 014005 (2015).

14. Cohen, J. et al. Recent Arctic amplification and extreme mid-latitude weather. Nat. Geosci. **7**, 627–637 (2014).

15. Cohen, J. et al. Divergent consensuses on Arctic amplification influence on midlatitude severe winter weather. Nature Climate Change **10**, 20–29 (2020).

16. Santer, B. D. et al. Identifying human influences on atmospheric temperature. Proceedings of the National Academy of Sciences **110**, 26–33 (2013).

17. Santer, B. D. et al. Human influence on the seasonal cycle of tropospheric temperature. Science **361**, (2018).

18. Chemke, R., Zanna, L. & Polvani, L. M. Identifying a human signal in the North Atlantic warming hole. Nature Communications **11**, 1540 (2020).

19. Blackport, R. & Kushner, P. J. Isolating the Atmospheric Circulation Response to Arctic Sea Ice Loss in the Coupled Climate System. J. Climate **30**, 2163–2185 (2017).

20. Sun, L., Deser, C. & Tomas, R. A. Mechanisms of Stratospheric and Tropospheric Circulation Response to Projected Arctic Sea Ice Loss. J. Climate **28**, 7824–7845 (2015).

21. Screen, J. A., Deser, C. & Sun, L. Reduced Risk of North American Cold Extremes due to Continued Arctic Sea Ice Loss. Bulletin of the American Meteorological Society **96**, 1489–1503 (2015).

22. Chripko, S. et al. Impact of Reduced Arctic Sea Ice on Northern Hemisphere Climate and Weather in Autumn and Winter. J. Climate, **34** 5847-5867 (2021).

23. Blackport, R. & Screen, J. A. Insignificant effect of Arctic amplification on the amplitude of midlatitude atmospheric waves. Science Advances **6**, eaay2880 (2020).

24. Shepherd, T. G. Atmospheric circulation as a source of uncertainty in climate change projections. Nat. Geosci. **7**, 703–708 (2014).

25. Tamarin-Brodsky, T., Hodges, K., Hoskins, B. J. & Shepherd, T. G. Changes in Northern Hemisphere temperature variability shaped by regional warming patterns. Nature Geoscience **13**, 414–421 (2020).

26. Managing the Risks of Extreme Events and Disasters to Advance Climate Change Adaptation: Special Report of the Intergovernmental Panel on Climate Change. (Cambridge University Press, 2012). doi:10.1017/CBO9781139177245.

27. Katz, R. W. & Brown, B. G. Extreme events in a changing climate: Variability is more important than averages. Climatic Change **21**, 289–302 (1992).

28. Vasseur, D. A. et al. Increased temperature variation poses a greater risk to species than climate warming. Proceedings of the Royal Society B: Biological Sciences **281**, 20132612 (2014).

29. Thornton, P. K., Ericksen, P. J., Herrero, M. & Challinor, A. J. Climate variability and vulnerability to climate change: a review. Global Change Biology **20**, 3313–3328 (2014).

Methods

Reanalysis and observations

We use daily-mean near-surface (2-meter) temperature data from two reanalysis products: ERA5 reanalysis[30] and NCEP-DOE reanalysis 2[31]. Data is used from March 1979 to February 2020, resulting in 41 years for each season. We also use gridded observations of daily near-surface temperature from Berkeley Earth[32] from March 1979 to February 2018. The observations from Berkeley Earth were only available up to 2018, but we chose to use reanalysis data up to 2020 to include the latest data.

Modelling experiments

We use output from large-ensemble climate model experiments from two models: the Canadian Earth System Model version 2 (CanESM2)[33,34] and the Community Earth System Model version 1 (CESM1)[35,36]. For CanESM2, four experiments with different forcings were performed: all-forcings (ALL), only anthropogenic aerosols (AER), only Natural forcings (NAT), and only stratospheric ozone forcings (OZ). Each experiment consists of 50 ensemble members with historical forcing from 1950 to 2005 and RCP8.5 forcing from 2006 to 2100. Historical emissions over 2006-2020 closely match the emissions from RCP8.5[37], justifying the comparison. Each of the 50 ensemble members was initiated from a different initial condition, so differences between ensemble members arise only due to internal variability. The response to anthropogenic greenhouse forcing is determined as a residual from subtracting the ensemble-mean trends of the AER, NAT and OZ from the ALL simulations. This approach means that land use changes are included in the response to anthropogenic greenhouse forcing for the CanESM2 simulations.

The CESM1 simulations consist of a 40-member all-forcing experiment, with historical forcing from 1920 2005 and RCP8.5 forcing from 2006 to 2100. The single forcing experiments from CESM1 were performed differently than those with CanESM2. These experiments were identical to the CESM1 all forcing ensemble, except one forcing at a time was held fixed at 1920 levels. Three such experiments were performed: a 20-member ensemble with fixed greenhouse gases, a 20-member ensemble with fixed industrial aerosols, and a 15-member ensemble with fixed biomass burning aerosols. The responses to individual forcings (Fig 4) were determined by subtracting the ensemble-mean of each of fixed forcing experiments from the ensemble mean of the all-forcing experiment.

Temperature variability calculation

All daily 2-meter temperatures from reanalysis, observations and models were first interpolated to a common 2°x 2° grid. We have confirmed that the results are insensitive to reasonable changes in the resolution that the analysis is performed on. Daily temperature anomalies were calculated by first subtracting the climatological (1979-2020) average temperature for each day and at each grid point. For model data, the climatological temperature was calculated separately for each ensemble member (not the ensemble mean) to be consistent with reanalysis and observations. Next, for each day and grid point, the linear trends over 1979-2020 period from the ensemble mean were removed. For reanalysis and observations, the mean of the two model's ensemble means were removed. Nearly identical results were obtained using other methods, including removing the linear trends from the ensemble-mean from each individual model, and removing the linear trend from each individual ensemble member, or from observations, or from reanalyses. For the model data, nearly identical results were also obtained if the daily ensemble-means were removed. For each year and season, the standard deviations of the daily temperature anomalies were calculated. This results in 41-year time-series of the subseasonal temperature variability at each grid point and each season.

Fingerprint and signal to noise calculations

We use standard fingerprint methods[16–18] to determine whether the signal is detectable in observations. First, we calculate the ensemble average of subseasonal temperature variability for each of the all-forcing experiments. Next, we calculate anomalies of temperature variability by subtracting the climatological mean at each grid-point. We then define the fingerprint to be the leading empirical orthogonal function (EOF) of the anomalies over all land grid points over the 30°-90°N latitude region for the 1979-2020 period. The results are not sensitive to the exact region chosen. The signal time-series are calculated by projecting the observed anomalies in temperature variability onto the fingerprint:

$$S(t)=\sum_{x=1}^{N_x} O(x,t)\cdot F(x)$$

Where S(t) is the signal time series, O(x,t) is the observed anomalies, F(x) is fingerprint, t represents the year, x represents the grid-point and N_x the number of grid-points. Fields are appropriately area-weighted prior to calculations by multiplying each grid-point by the square root of the cosine of the latitude.

The noise time-series are calculated by first subtracting the appropriate ensemble-mean of the temperature variability time-series from individual ensemble members of the ensemble (including all single forcing experiments). Next, each of these time-series are then projected onto the fingerprint, as was done for observed anomalies in the equation above. This results in 200 41-year noise time-series for CanESM2 and 95 41-year noise time-series for CESM1. These noise time-series consist only of unforced internal variability.

To calculate whether the observed trends are statistically significant, we calculate the signal-to-noise ratios. Here, the signal is defined as the magnitude of the linear trend of the observed signal time-series. The noise is defined as the standard deviation of the distribution of linear trend magnitudes of the noise time-series of the same length as the signal. Signal-to-noise ratios are calculated as a function of increasing trend length for trends starting in 1979, with a minimum trend length of 15 years. We define statistical significance to be a signal-to-noise ratio of 1.645, which is the 5% significance threshold using a one-sided Students t-test. The time of detection is determined by the first year where the signal-to-noise ratio exceeds and subsequently remains above this level.

References

30. Hersbach, H. et al. The ERA5 global reanalysis. Quarterly Journal of the Royal Meteorological Society **146**, 1999–2049 (2020).

31. Kanamitsu, M. et al. NCEP–DOE AMIP-II Reanalysis (R-2). Bull. Amer. Meteor. Soc. **83**, 1631–1644 (2002).

32. Rohde, R. A. & Hausfather, Z. The Berkeley Earth Land/Ocean Temperature Record. Earth System Science Data **12**, 3469–3479 (2020).

33. Arora, V. K. et al. Carbon emission limits required to satisfy future representative concentration pathways of greenhouse gases. Geophysical Research Letters **38**, (2011).

34. Kirchmeier-Young, M. C., Zwiers, F. W. & Gillett, N. P. Attribution of Extreme Events in Arctic Sea Ice Extent. J. Clim. **30**, 553–571 (2016).

35. Hurrell, J. W. et al. The Community Earth System Model: A Framework for Collaborative Research. Bull. Amer. Meteor. Soc. **94**, 1339–1360 (2013).

36. Kay, J. E. et al. The Community Earth System Model (CESM) Large Ensemble Project: A Community Resource for Studying Climate Change in the Presence of Internal Climate Variability. Bull. Amer. Meteor. Soc. **96**, 1333–1349 (2015).

37. Schwalm, C. R., Glendon, S. & Duffy, P. B. RCP8.5 tracks cumulative CO2 emissions. PNAS **117**, 19656–19657 (2020).

Data Availability

CanESM2 data is available at: https://open.canada.ca/data/en/dataset/aa7b6823-fd1e-49ff-a6fb-68076a4a477c. CESM1 data is available at: https://www.earthsystemgrid.org/dataset/ucar.cgd.ccsm4.CESM_CAM5_BGC_LE.html. ERA5 reanalysis data is available at: https://cds.climate.copernicus.eu/cdsapp#!/dataset/reanalysis-era5-single-levels?tab=overview. NCEP-DOE reanalysis 2 data is available at: https://psl.noaa.gov/data/gridded/data.ncep.reanalysis2.html. Berkeley Earth observations are available at: http://berkeleyearth.org/archive/data/.

Code availability

Code is available form the corresponding author upon reasonable request.

Acknowledgments: We thank the Canadian Centre for Climate Modelling and Analysis and the National Center for Atmospheric Research for performing the large ensemble simulations and making the data available. We also thank the European Centre for Medium Range Weather

Forecasts, the National Center for Environmental Prediction, and Berkeley Earth for making the reanalysis and observational datasets available.

Author Contributions: R.B. conceived of the study, carried out the analysis, and wrote the manuscript. J.C.F and J.A.S. discussed the results and made suggestions and edits to the manuscript.

Competing Interests: The authors declare no competing interests.

Correspondence and request for materials should be addressed to R.B.

Figures

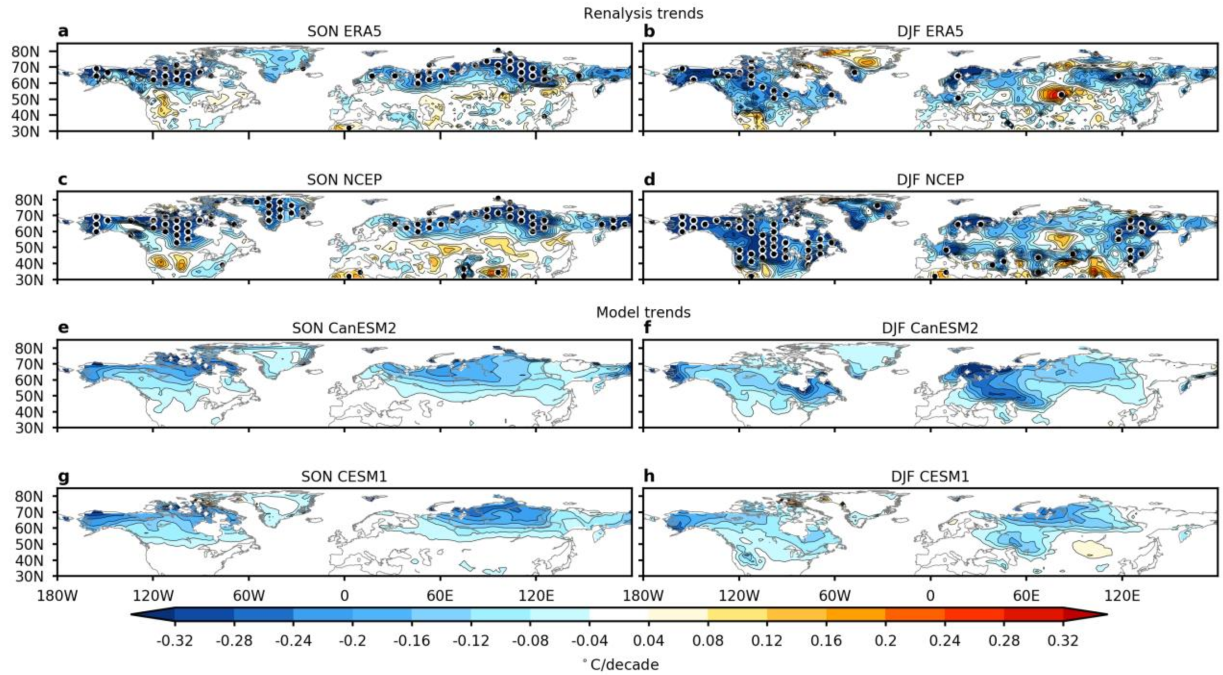

Figure 1: Subseasonal near-surface temperature variability trends. Trends in subseasonal near-surface air temperature variability (°C/decade) in autumn (SON; a, c, e, g) and winter (DJF; b, d, f, h) over the 1979-2020 period. Trends are shown for ERA5 reanalysis (a, b) NCEP reanalysis (c, d), CanESM2 simulations (e, f) and CESM1 simulations (g, h). The stippling in a-d indicates trends that are statistically significant at the 5% level using a two-sided student's t-test.

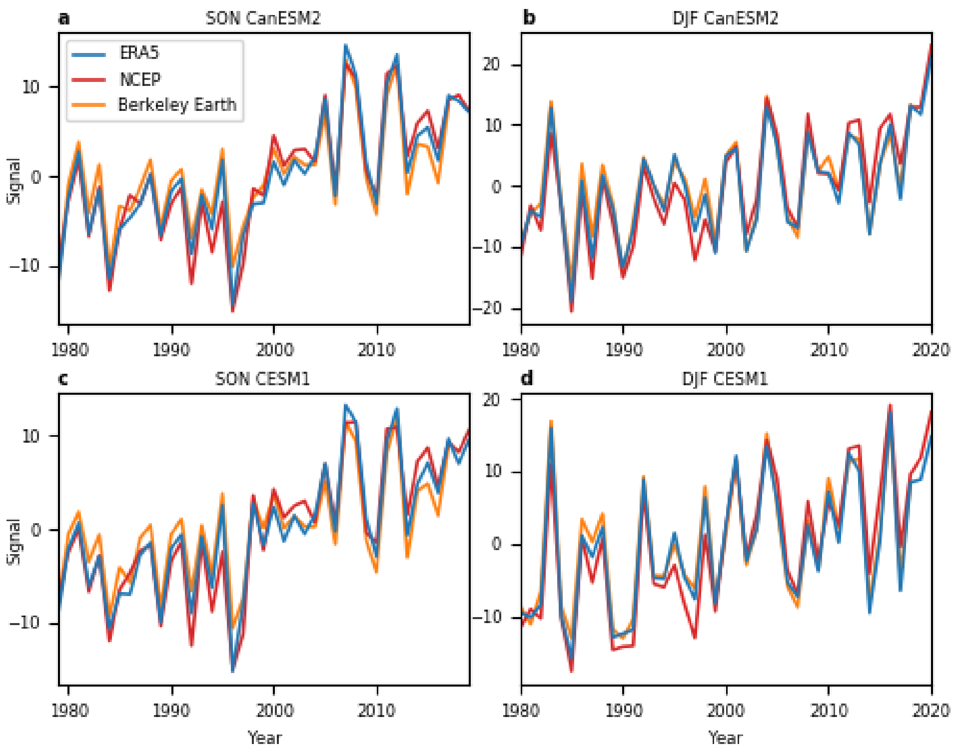

Figure 2: Signal time-series of the subseasonal temperature variability fingerprint. Signal time-series of the subseasonal temperature variability fingerprint in the ERA5 reanalysis (blue), NCEP reanalysis (red) and Berkeley Earth observations (orange). Time series are shown for autumn (SON; a, c), winter (DJF; b, d) and for the fingerprint calculated from the CanESM2 simulations (a, b) and CESM1 simulations (c, d).

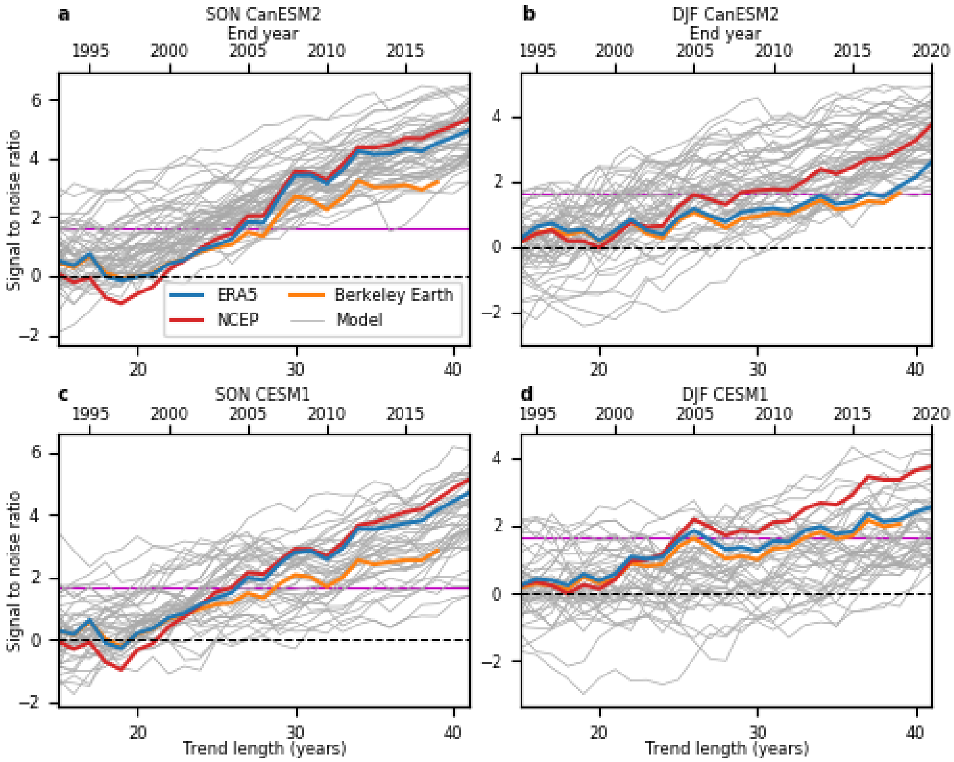

Figure 3: Signal-to-noise ratios for increasing trend length. Signal-to-noise ratios as a function of trend length for trends starting in 1979/80, for the ERA5 reanalysis (blue), NCEP reanalysis (red) and Berkeley Earth observations (orange), and individual model realizations (grey). Signal-to-noise ratios are shown for autumn (SON; a, c), winter (DJF; b, d) and for the fingerprint calculated from the CanESM2 simulations (a, b) and CESM1 simulations (c, d). The purple line indicates statistical significance at the 5% level. Note the different vertical axes in the different panels.

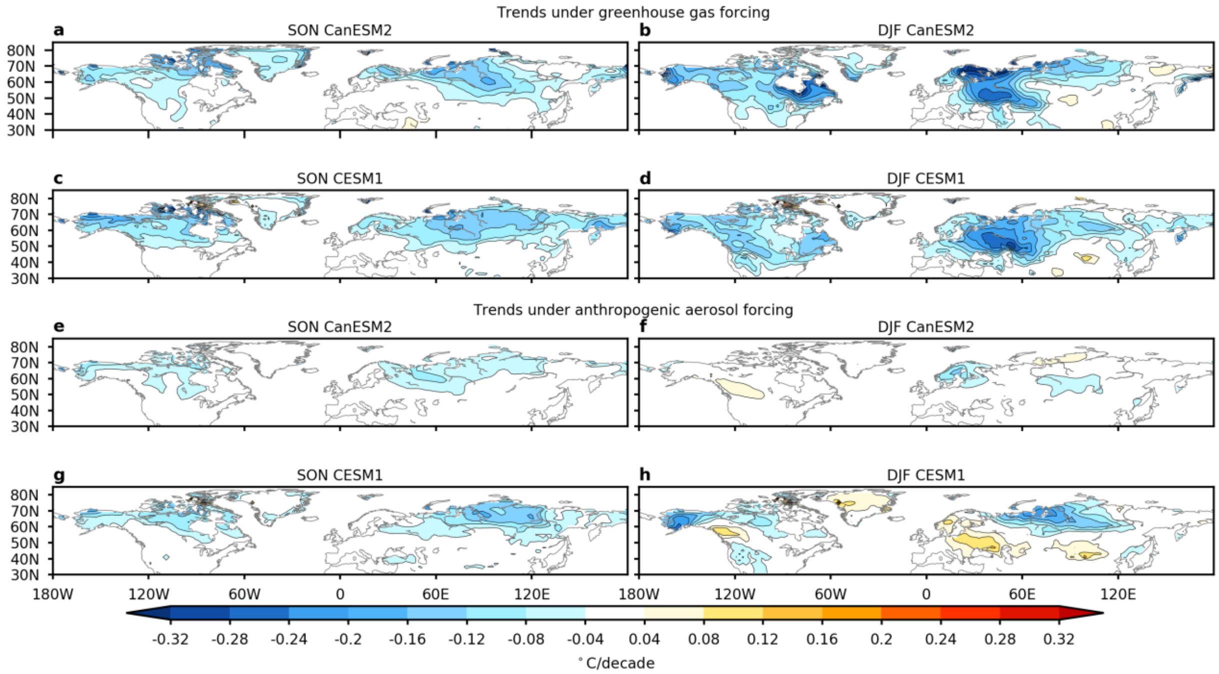

Figure 4: Drivers of subseasonal temperature variability trends. Trends in subseasonal near-surface air temperature variability (°C/decade) in autumn (SON; a, c, e, g) and winter (DJF; b, d, f, h) over the 1979-2020 period from the single-forcing experiments. Trends are shown for anthropogenic greenhouse gas forcing (GHG; a-d), anthropogenic aerosol forcing (AER; e-h), in CanESM2 simulations (a, b, e, f) and CESM1 simulations (c, d, g, h).

Extended Data Figures

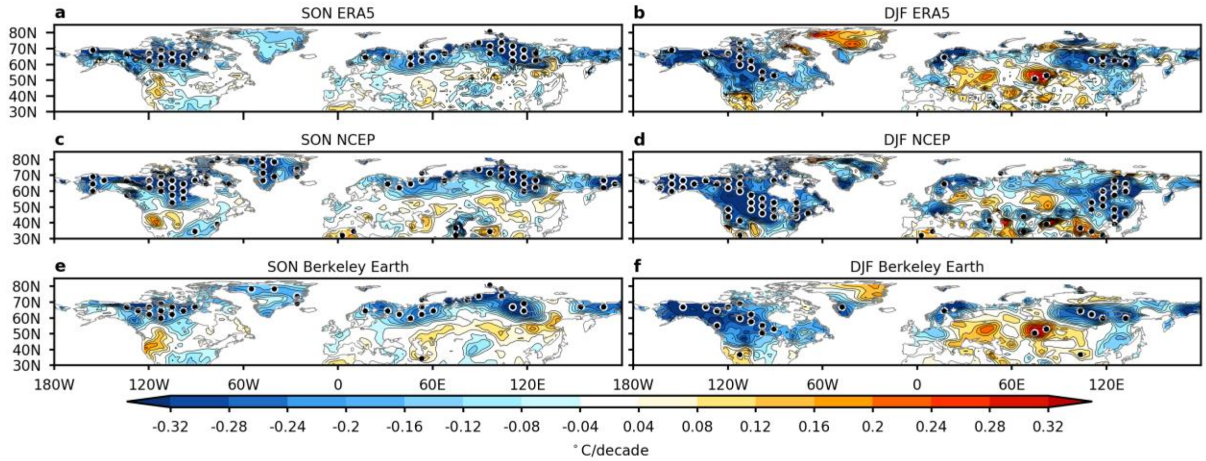

Extended Data Figure 1: Subseasonal near-surface temperature variability trends in reanalysis and observations. Trends in subseasonal near-surface air temperature variability (°C/decade) in autumn (SON; a, c, e) and winter (DJF; b, d, f) over the 1979-2018 period. Trends are shown for ERA5 reanalysis (a, b) NCEP-DOE-reanalysis 2 (c, d), and Berkeley Earth observations (e, f). The stippling indicates trends that statistically significant at the 5% level using a two-sided student's t-test.

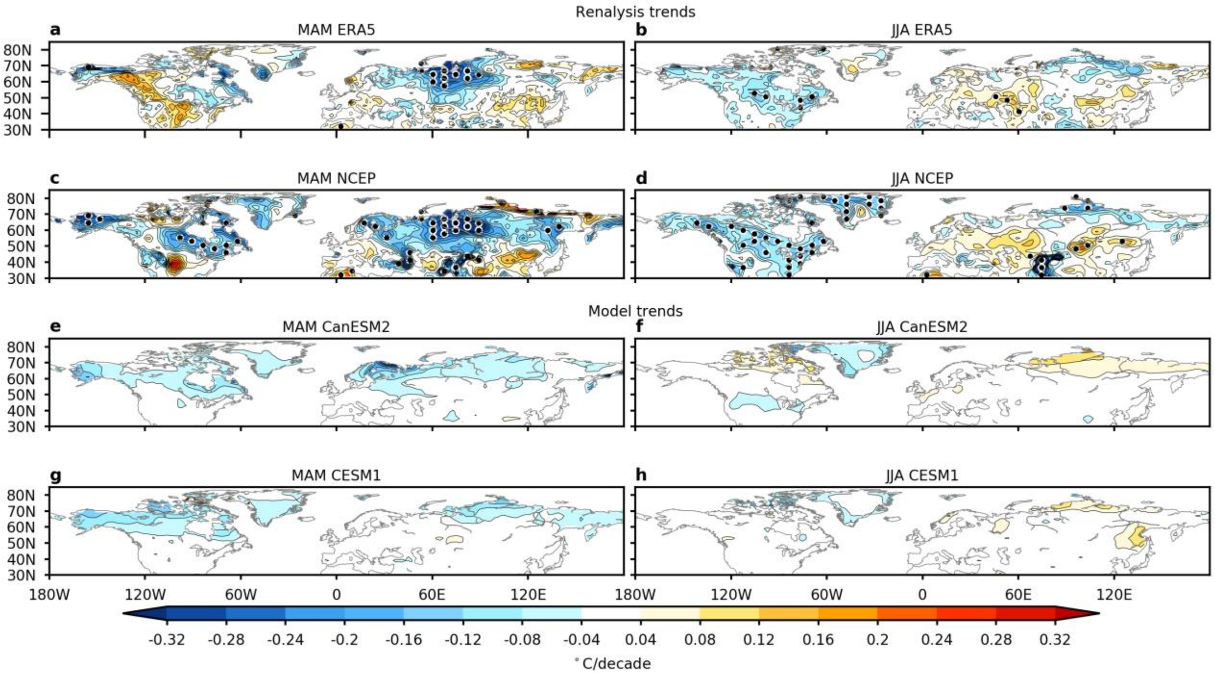

Extended Data Figure 2: Subseasonal near-surface temperature variability trends in spring and summer. As in Fig 1, but for spring (MAM) and summer (JJA).

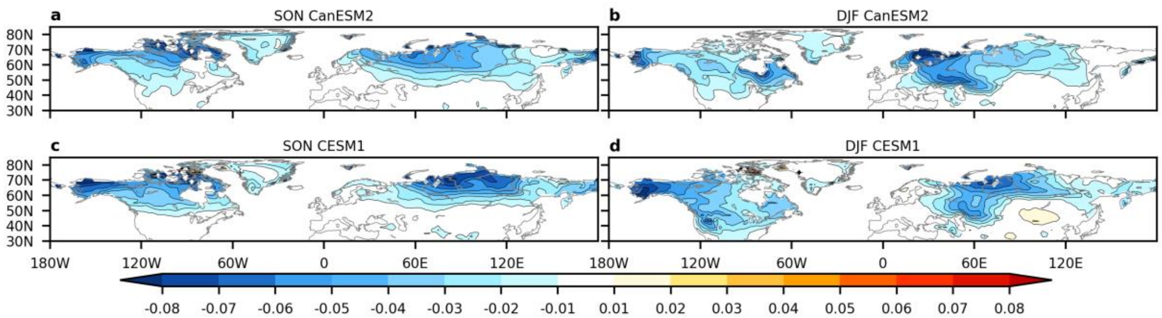

Extended Data Figure 3: Fingerprints of subseasonal temperature variability. The fingerprints of subseasonal temperature variability from CanESM2 (a, b) and CESM1 (c, d) for autumn (SON; a, c) and winter (DJF; b, d).

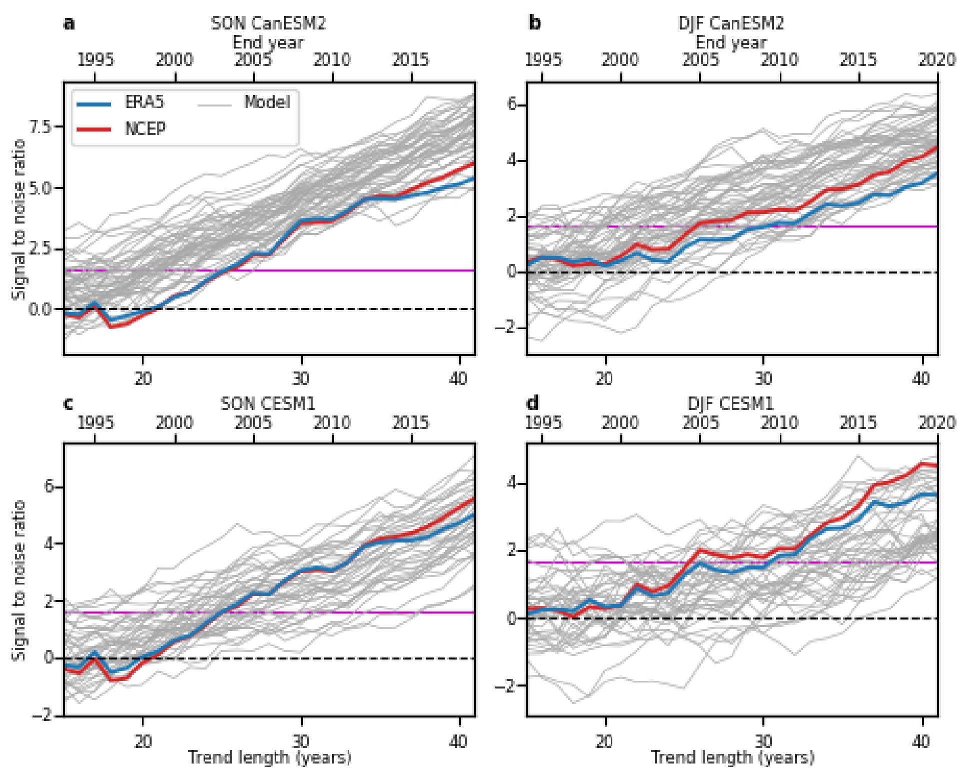

Extended Data Figure 4: Signal-to-noise ratios for increasing trend length. As in Fig 3, but with grid-points over ocean included in the fingerprint.

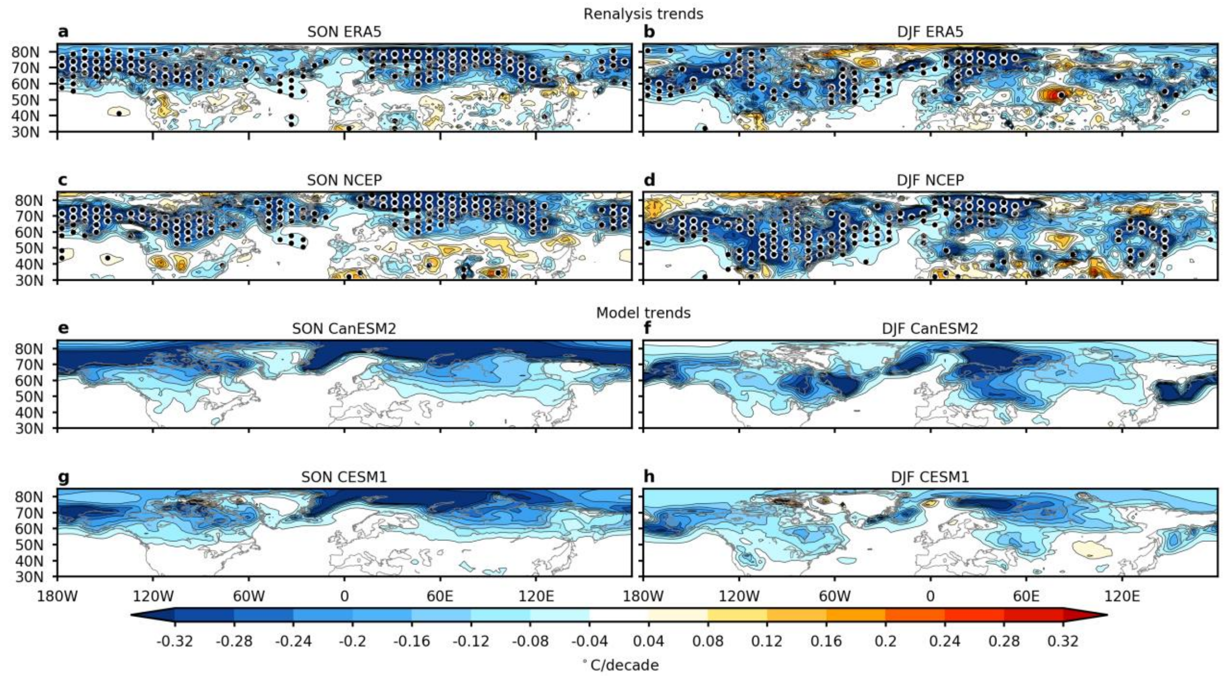

Extended Data Figure 5: Subseasonal near-surface temperature variability trends. As in Fig 1, but with grid points over ocean included.

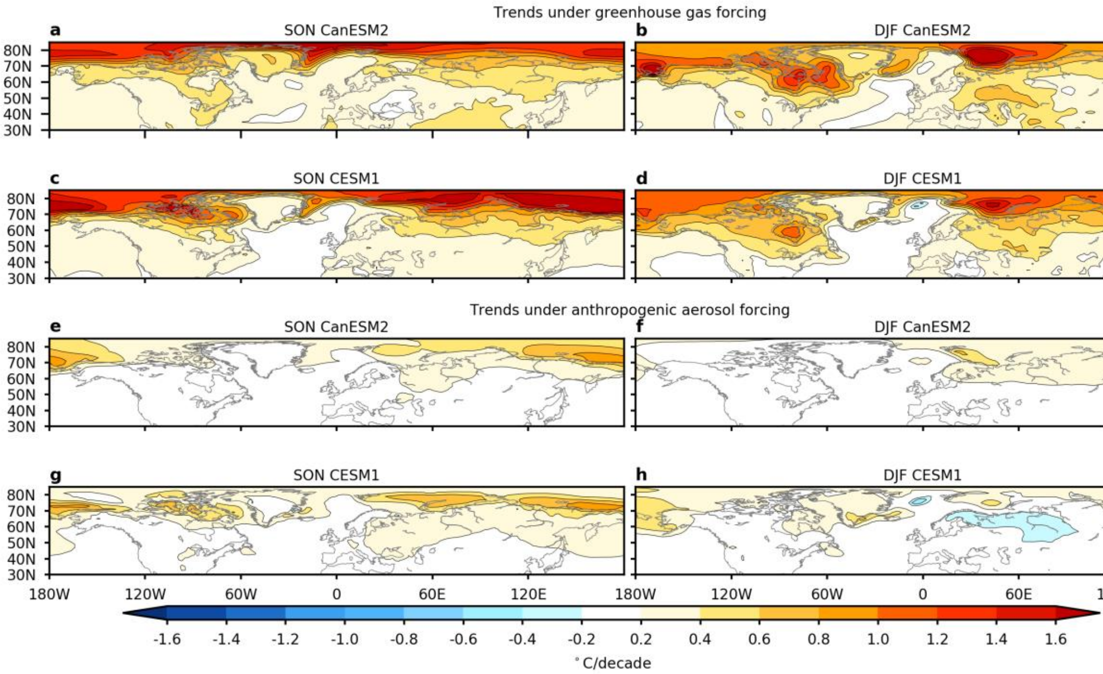

Extended Data Figure 6: Seasonal-mean near-surface temperature trends. As in Fig 4, but for seasonal-mean temperature trends (°C/decade).

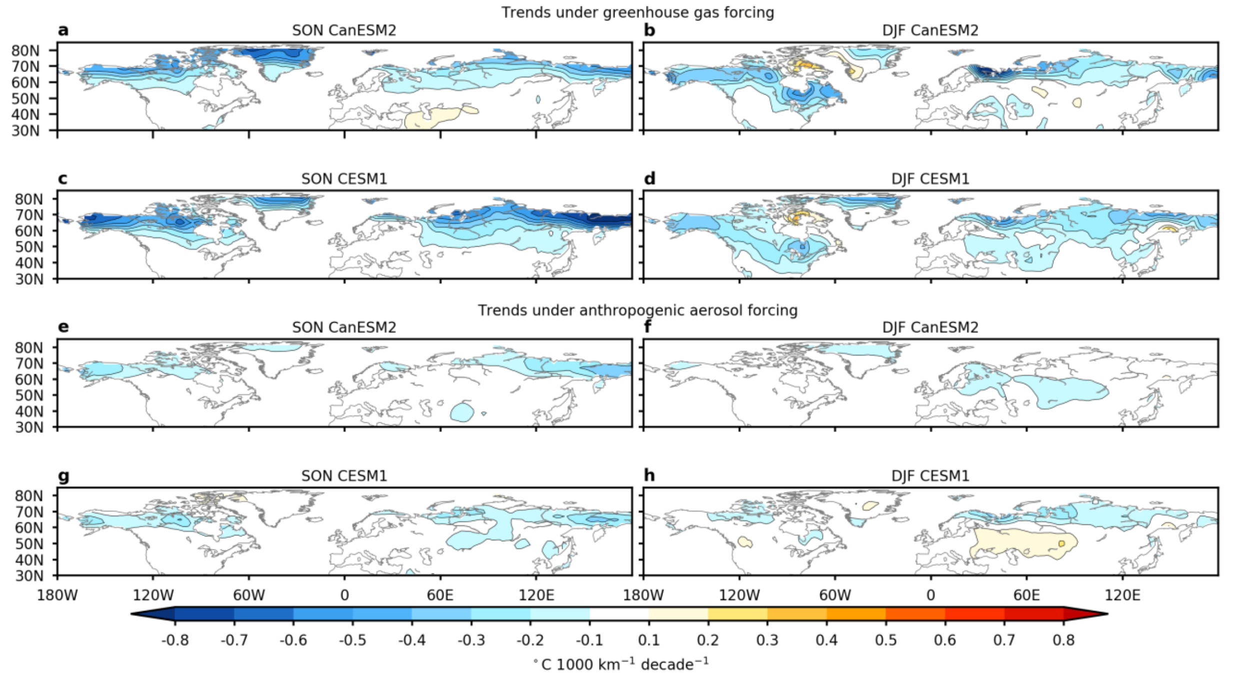

Extended Data Figure 7: Meridional temperature gradient trends. As in Fig 4, but for meridional temperature gradient trends (°C 1000 km^{-1} decade^{-1}).